



Spectroscopic and Thermal Analysis of CuO–ZnO Composite Particles Synthesized by Sol-Gel Method

Davaadulam BATBILEG¹, Narangerel ADIYASUREN¹,
Erdene NOROV¹, Tseelei SUREN², and
Ganzorig CHIMED¹

¹ Center for Nanoscience and Nanotechnology, Department of Chemical and Biological Engineering, School of Engineering and Technology, National University of Mongolia, Ulaanbaatar 14201, Mongolia

² Department of Basic Sciences, Erdenet Institute of Technology, Mongolian University of Science and Technology, Erdenet 61027, Mongolia

³ davaadulambatbileg@gmail.com

Abstract. Photocatalysis is a green technology that plays a vital role in achieving sustainable development goals and ensuring a clean environment. Metal oxide materials, in particular, have gained tremendous attention for their versatility in fields such as catalysis, semiconductors, ceramics, sensors, and energy storage. In this work, the sol-gel method has been used to synthesize CuO–ZnO composite particles. To understand their structural transformations, CuO–ZnO composite materials' thermal decomposition and phase evolution. Thermal analysis is crucial for determining the optimal calcination temperature during synthesis. We studied mass loss and phase transitions to identify the temperature, which affects vital photocatalytic parameters including crystallization, particle size, and surface area. To examine thermal stability and temperature-specific mechanisms, we analyzed samples dried at 120°C and 500°C using Thermogravimetry-Differential Thermal Analysis (TG-DTA), Fourier-transform infrared spectroscopy (FTIR), and X-ray diffraction (XRD). Thermal kinetic evaluation using the Coats–Redfern method resulted in an activation energy of 38.63 kJ/mol with a strong correlation coefficient of $R^2=0.94$, indicating reliable thermal decomposition behavior. These values reflect moderate thermal stability, which is favorable for the formation of active photocatalytic phases without excessive energy input. We then characterized the composite's chemical composition using Raman spectroscopy while examining its optical and morphology properties through Ultraviolet-visible (UV-Vis) spectroscopy and Atomic force microscopy (AFM). These findings contribute to understanding the thermal stability, crystallization behavior, and phase interactions of CuO–ZnO composites, supporting their use in photocatalysis and functional materials. The results contribute to a better understanding of the temperature-dependent transformations in CuO–ZnO materials and provide a quantitative basis for their potential applications in photocatalysis and multifunctional materials. Future work will aim to include naturally occurring Cu₂O phases in the composite structure to improve green photocatalytic efficiency and expand the use of the material in cleaning up the environment.

Keywords: photocatalytic, thermal decomposition, sol-gel method

© The Author(s) 2025

A. Lkhamsuren et al. (eds.), *Proceedings of the 3rd International Conference Resources and Technology (RESAT 2025)*, Advances in Engineering Research 284,

https://doi.org/10.2991/978-94-6463-928-5_2

1 Introduction

Recently, the environmental pollution levels from chemical, soil, and air pollution have exceeded planetary boundaries, which put at risk for entire ecosystems [1-2]. Photocatalysis, widely employed in water and air purification, self-cleaning surfaces, antibacterial coatings, energy production, and the food industry, is based on the principle of excitation, in which a photon excites an electron from the valence band to the conduction band of a semiconductor, leaving behind a hole in the valence band [3-8]. Photocatalytic reactions on metal oxide semiconductors can degrade many pollutants and are, thus, of great interest [3]. Photogenerated charge carriers formed through band gap excitation can reduce or oxidize species adsorbed on the semiconductor material. However, the high degree of recombination of charge carriers is a disadvantage [4]. Among the transition metal oxides, copper oxide (CuO) belongs to the group of p-type transition metal oxides with a monoclinic crystal structure and semiconductor properties at high critical temperatures [5]. It is a semiconductor with a band gap of 1.2-1.8 eV [6]. To synthesize copper oxide with various morphologies and dimensions, methods such as thermal evaporation, sonochemical synthesis, sol-gel, hydrothermal, electrochemical, and microwave radiation techniques are used. Among these, the sol-gel method stands out due to its simplicity, cost-effectiveness, and high efficiency. For example, CuO can be synthesized by calcining a precipitate formed from a Cu(II) salt solution at high temperatures. The phase size and shape of the precipitated material largely depend on the chemical characteristics of the Cu(II) complexes in the gel solution, which can be controlled. These characteristics depend on factors such as the type and concentration of complexing anions and the pH of the solution. The addition of organic or inorganic additives such as urea, polyethylene glycol, and polyvinyl can guide the precipitation and reaction processes, enabling the formation of CuO with a desired structure [12-13].

Zinc oxide (ZnO) is an n-type transition metal semiconductor with a wide band gap of 3.37 eV and exhibits multiple properties such as semiconductivity, piezoelectricity, and pyroelectricity, making it a unique material [9]. In addition to the wurtzite structure, ZnO can also exist in zinc blends and very rarely in cubic rock salt forms. The wurtzite structure is the most stable, in which anions are surrounded by four cations forming a tetrahedral structure with sp^3 hybridization in a hexagonal close-packed lattice [10]. ZnO is often used as a catalyst, and its catalytic properties can be enhanced by forming composites with other metals. For example, Schlögl and co-workers prepared a CuZnO catalyst from hydroxycarbonate [11]. In another study, Karelavic synthesized a Cu-ZnO catalyst via the decomposition of citric acid [12]. Over the past decade, metal oxide composites have attracted significant attention from researchers in various fields such as physics, chemistry, and materials science due to their wide practical applications in semiconductors, photocatalysts, sensors, microelectronics, piezoelectric devices, and biofuels [18-21]. Among the various synthesis methods, the sol-gel process is favored for its simplicity, low cost, efficiency, and environmental friendliness. It also allows control over the doping process and the morphology of the materials [22-23]. Photocatalysis, especially

heterogeneous photocatalysis, is one of the most investigated processes for environmental remediation. Indeed, the use of solar light, which is an infinite source of energy, to activate photocatalysts is a sustainable technology [38]. Another alternative to obtain visible-light-assisted reactions is through the combination of semiconductor and noble metal nanoparticles; these are the so-called plasmonic photocatalysts [39]. Such photocatalytic processes have two major impacts in green technology: (i) environmental remediation, including the degradation of toxic organic dyes and pollutants in wastewater into harmless by-products, and (ii) renewable energy generation, such as photocatalytic water splitting for hydrogen production and CO₂ photoreduction into solar fuels. In particular, the combination of ZnO and CuO into a composite semiconductor is expected to enhance charge separation, extend visible-light absorption, and improve surface reactivity, thereby bridging both environmental and energy-related applications. Our previous work by Ts. Nomin et al. investigated using copper oxide nanocomposites [40]. Building on this, we are particularly interested in copper oxide and other metal oxide composites. The present study therefore aims to examine the characteristics of these materials, with a specific focus on their photocatalytic applications.

One type of sol-gel method, the Pechini process, utilizes the chelating ability of certain alpha-hydroxycarboxylic acids with metal ions. In a typical synthesis, metal salts are dissolved in water with citric acid and ethylene glycol, resulting in a homogeneous solution containing metal-citrate chelate complexes. Upon heating, citric acid and ethylene glycol react to form polyesters through covalent bonding.

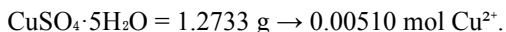
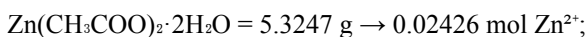
This study aims to synthesize CuO–ZnO composite materials via the sol-gel method and to examine how thermal treatment and phase transitions influence their physicochemical properties and structural formation. The composite was synthesized via the Pechini method by heating at 500°C. The CuO–ZnO composite showed the highest absorption at 373 nm with a band gap energy of 2.8 eV. Morphologically, the particles aggregated to form a spherical structure. Since the decomposition of the precursors begins at 400°C, the sample was calcined at 500°C to obtain the composite material. XRD analysis confirmed the formation of monoclinic CuO and hexagonal ZnO structures, indicating the formation of spherical composites. Spectroscopic and thermal analyses were conducted to study the composite formation temperature, intermolecular bonding, morphology, and surface changes.

2 Experimental

2.1 Synthesis of CuO–ZnO composite

Synthesis of CuO–ZnO composite used the sol-gel method [20]. Firstly, 25 mL of ethylene glycol was mixed with 5.3247 g of Zn(CH₃COO)₂·2H₂O, 25 mL of distilled water, and 6.3 g of citric acid with vigorous stirring for an hour. After an hour, 1.2733 g of CuSO₄·5H₂O was added to the suspension at 60°C for 3 hours and

mixed quickly. The solution was kept in the dark for 48 hours and washed with distilled water several times. The obtained gel was dried at 120°C to constant weight and calcined at 500°C for 4 hours to produce the CuO–ZnO composites. The precursor concentrations were selected to achieve the targeted stoichiometry of the final CuO–ZnO composite while ensuring homogeneous mixing at the molecular scale during the Pechini sol–gel process. The $\text{CuSO}_4 \cdot 5\text{H}_2\text{O} : \text{Zn}(\text{CH}_3\text{COO})_2 \cdot \text{H}_2\text{O}$ ratio of 1:3 was chosen to (i) modulate the band gap into the visible-light absorption region, (ii) balance the conduction and valence band positions for effective charge separation, and (iii) control the morphology by influencing nucleation and growth rates during gel combustion and calcination. Higher Cu precursor concentration typically promotes the formation of smaller, more aggregated particles due to the lower thermal stability of CuO nuclei, whereas higher Zn precursor content favors elongated wurtzite ZnO crystallites. The final stoichiometry was confirmed by quantitative phase analysis of the calcined powders using XRD data. We targeted a CuO–ZnO heterojunction with visible-light absorption and efficient charge separation. Based on the weighed salts:



Thus, the feed molar ratio was $\text{Cu}:\text{Zn} \approx 0.21:1$ ($\approx 1:4.76$), which would yield a theoretical oxide fraction of ≈ 17 wt% CuO and 83 wt% ZnO after calcination, assuming quantitative conversion.

2.2 Mechanism of composite formation

1. Chelation – Formation of Chelate Complexes: An aqueous solution containing metal oxides is mixed with an alpha-hydroxycarboxylic acid such as citric acid. This acid acts as a chelating agent, forming ring-like chelate complexes with the metal cations present in the solution.
2. Polymerization: Next, a polyhydroxy alcohol such as ethylene glycol is added to the mixture. Upon heating, the chelate complexes undergo polymerization, leading to the formation of a polymeric network.
3. Gel Formation: As heating continues and excess water evaporates, a gel is formed that contains a solid polymer matrix with evenly distributed metal cations.
4. Calcination: The gel is then calcined at elevated temperatures, typically between 500°C–900°C. This thermal treatment decomposes the organic components and results in the formation of the metal oxide composite. The resulting particles typically range in size from 20 to 50 nanometers, though larger aggregates may form due to particle agglomeration [26–27].

3 Results and Discussion

3.1 Molecular Spectroscopic Characterization

3.1.1 Determination of Band Gap Energy via UV-Vis Spectroscopy

The UV-Visible absorption spectrum of the CuO–ZnO composite is presented in Figure 1. The sample was ultrasonically dispersed in deionized water at a 1:100 ratio and measured in the wavelength range of 250–700 nm. The absorption peak was observed at 373 nm. Based on this result, the optical band gap energy was estimated to be 2.8 eV using Tauc's relation. The Tauc equation (3.1) describes the relationship between the optical absorption coefficient and the electronic transition across the band gap. The formation of the CuO–ZnO composite leads to a narrowing of the band gap, which is attributed to hybridized transitions from O^{2-} (2p) orbitals to Zn^{2+} (3d¹⁰-4s) and Cu^{2+} (3d⁹) states [20]. The reduced band gap energy suggests that the CuO–ZnO composite possesses enhanced photocatalytic activity compared to the individual oxides, CuO and ZnO.

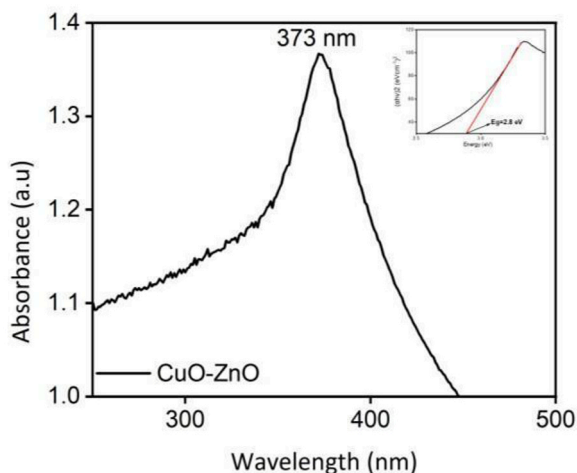


Fig. 1. UV-Vis spectrometry absorption value and band gap.

3.1.2 Results of Molecular Interaction Analysis Using Raman Spectroscopy

Raman spectroscopy is a molecular spectroscopic technique based on the interaction mechanism between light waves and matter, used to determine the structure and properties of materials. Raman spectroscopy measures intra- and intermolecular vibrations. In this study, the Resonance Micro Raman spectrum of the Department of Physics of the State University of Technology of Mongolia was obtained using a NRS 5500 spectrometer equipped with a solid-state green laser generator with a wavelength of 532–1100 nm and a confocal optical microscope with a

magnification of 100 times. The cross-sectional diameter of the laser spot was approximately $2\ \mu\text{m}$, and the Raman spectrum was obtained with a diffraction grating with a grating constant of 1800 lines/mm with a resolution of $1\ \text{cm}^{-1}$. For the measurements, a thin layer was formed on a glass substrate, and a 25 mW laser was used. The results of the Raman spectra of the sample obtained are shown in Figure 2.

The results indicate peaks at $278\ \text{cm}^{-1}$, $416\ \text{cm}^{-1}$, $564\ \text{cm}^{-1}$, and $1096\ \text{cm}^{-1}$, suggesting the formation of a CuO–ZnO composite. According to previous studies, the CuO–ZnO composite typically exhibits peaks at $277.40\ \text{cm}^{-1}$, $324.96\ \text{cm}^{-1}$, $426.6\ \text{cm}^{-1}$, $591.38\ \text{cm}^{-1}$, $609.50\ \text{cm}^{-1}$, and $1067.69\ \text{cm}^{-1}$ [23].

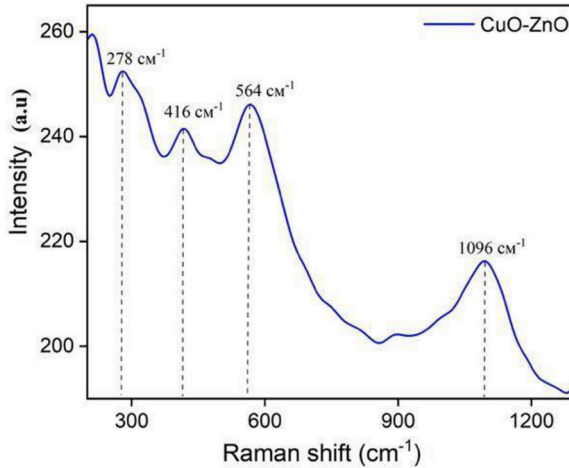


Fig. 2. Raman spectra of CuO–ZnO.

Monoclinic CuO, which has a centrosymmetric $C2h6$ space group, displays optical phonon modes in the A_g and $2B_g$ stretching regions, with characteristic peaks at $296\ \text{cm}^{-1}$, $346\ \text{cm}^{-1}$, and $636\ \text{cm}^{-1}$ [24]. According to the findings of Wang et al., three peaks at $380\ \text{cm}^{-1}$, $436\ \text{cm}^{-1}$, and $576\ \text{cm}^{-1}$ correspond to the A_{1T} , E_{2H} , and A_{1L} stretching modes, respectively [12].

3.2 Study of Morphological Changes using AFM

Figure 3 presents two-dimensional and three-dimensional images captured over $0.3\ \mu\text{m} \times 0.3\ \mu\text{m}$. The AFM analysis reveals an uneven distribution with spherical-shaped CuO–ZnO particles that are aggregated and interconnected. From the area depicted in Figure 4, cross-sectional measurements were performed on 20 selected points, yielding an average particle size of $13.18\ \text{nm}$.

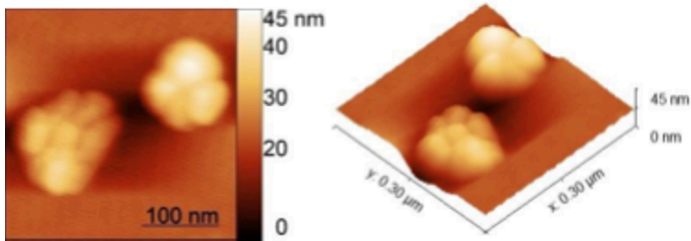


Fig. 3. AFM image of CuO–ZnO composite.

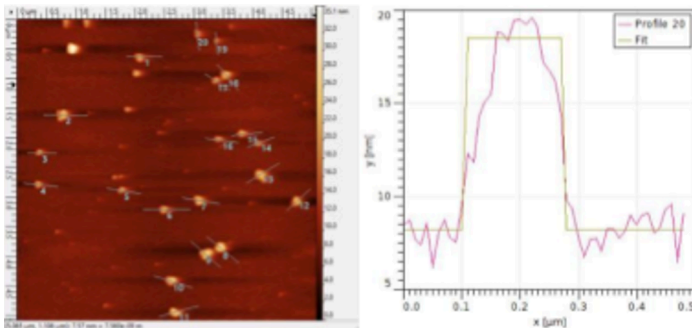


Fig. 4. Cross-sectional view of the AFM image.

Figure 5 shows the values of the measured regions of the AFM line profile at $n=5$. The mean value was 14.37 nm, with a standard deviation of ± 2.64 nm ($n = 5$). The standard error of the mean was 1.18 nm, giving a 95% confidence interval of 14.37 ± 3.27 nm. Also, the corresponding uncertainty (± 1.7 – 3.9 nm). The mean value (13.18 nm) shown in Figure 4 is within the 95% CI determined from the 5 parameter values. The calculation data and results are shown in Table 1.

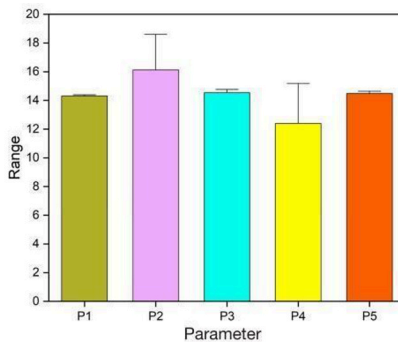


Fig. 5. AFM step height measurements error bar (n = 5).

Table 1. Statistic calculation.

Term / Formula	Calculation
Data (xi)	14.246, 17.872, 14.693, 10.432, 14.595
Mean (\bar{x}) = $\Sigma xi / n$	14.37
Deviation ($xi - \bar{x}$)	-0.122, 3.504, 0.325, -3.936, 0.227
Squared deviation ($xi - \bar{x}$) ²	0.015, 12.281, 0.106, 15.489, 0.052
$\Sigma (xi - \bar{x})^2$	27.94
Variance = $\Sigma(xi - \bar{x})^2 / (n-1)$	6.99
Standard Deviation (SD) = $\sqrt{\text{Variance}}$	2.64

3.3 Thermal and Structural Analysis

3.3.1 Results of Mass Change Determination Using TG-DT

Thermogravimetric analysis (TG) is a technique used to measure the change in mass of a substance as a function of temperature by heating the sample under controlled conditions. In the synthesis of the CuO–ZnO composite, the material was first dried at 120°C for dehydration and then further heated to 500°C to form the composite. Thermal analysis methods were employed to study the thermal stability of the composite and the mechanisms occurring at specific temperatures. Each sample, dried at 120°C and 500°C respectively, was heated up to 1000°C at a heating rate of 20°C/min, and the results are presented in Figures 6a-b and Figure 7.

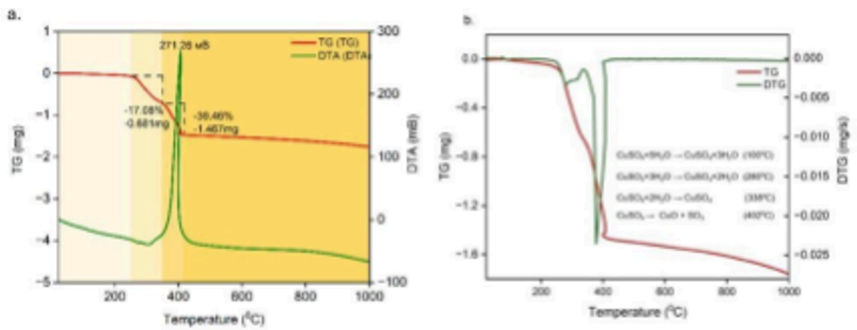


Fig. 6. Thermal analysis of a sample dried at 120°C. (a) Relationship between mass change and heat flow, (b) thermal decomposition of the material – mass change.

Figure 6a displays the mass change and heat flow as functions of temperature. According to the graph, a significant mass loss occurs between 280°C and 400°C, with a total reduction of 39.46%. The decomposition process is observed to be exothermic, as indicated by the thermal flow curve. The decomposition of citric acid

produces by-products such as H₂O (Equation 3.1) and CO₂ (Equation 3.2) [25-26]. This decomposition plays a key role in the formation of the organic matrix. The phases resulting from the mass loss have been color-coded to indicate phase transitions. The thermal decomposition process can be divided into two main stages: dehydration (25°C-200°C) and decomposition of residual organic compounds (200°C-400°C) [27].

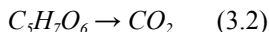
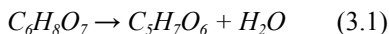


Figure 6b presents the derivative thermogravimetric (DTG) curve, which expresses the rate of mass loss as a function of temperature and reflects the thermal decomposition rate of the material. The mass loss and decomposition rates during thermal degradation are summarized in Table 2. Water loss in the sample occurs in multiple stages. For the copper compound, the initial stage of dehydration occurs at approximately 150°C, while for the zinc compound, it begins around 140°C. The second stage of copper decomposition starts above 200°C and completes near 500°C. In the case of zinc, this stage is confirmed by a change in the decomposition rate around 450°C, which is more prominently visible in the DTG curve [28-29].

Table 2. Thermal decomposition rate and mass change.

Temperature range	25-100°C	100-280°C	280-340°C	340-402°C
Mass change	-0.01 mg	-0.237 mg	-0.668 mg	-1.276 mg
Decomposition rate	-	-0.003 mg/s	-0.001 mg/s	-0.013 mg/s

The mass loss observed on the thermogravimetric (TG) curve below 300°C is attributed to the release of water molecules formed during the esterification process. The mass loss up to 400°C is related to the products generated during oxidation and decomposition reactions. Above 400°C, the minimal mass loss is associated with the crystallization process [22]. Figure 7 presents the thermal analysis results of the sample dried at 500°C. When heated up to 1000°C, 96% of the sample mass remained, indicating high thermal stability. As the temperature increases, oxygen release becomes more pronounced, and a new phase forms as a result of the reaction between two existing phases, as shown in Equation 3.3 [30-31]:

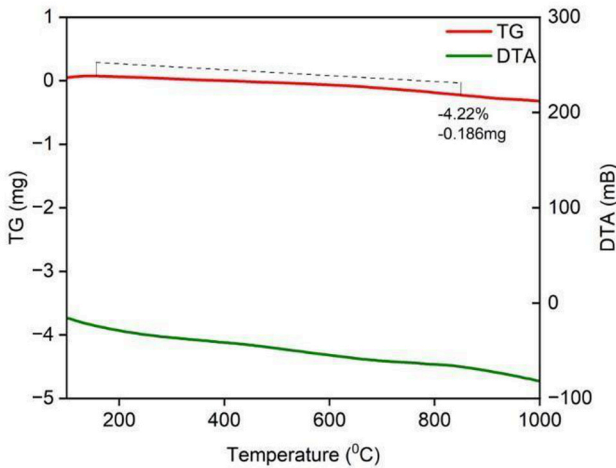
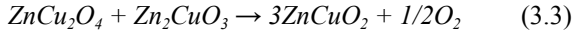


Fig. 7. Thermal analysis of samples dried at 500°C.

Kinetic Analysis using the Coats–Redfern Method

To further investigate the thermal decomposition behavior of the CuO–ZnO composite, kinetic analysis was performed using the Coats–Redfern method (Equation 3.4-3.5). The Coats-Redfern integral method can deal with the reaction kinetics at a constant heating rate; therefore, Coats-Redfern integration method is also employed for comparative kinetic analysis [32-33].

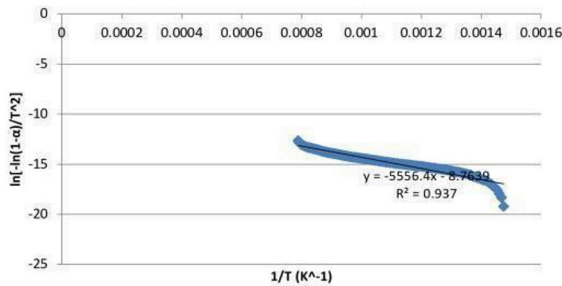


Fig. 8. Coats-Redfern plot

The most significant mass loss region observed in the TG curve at a heating rate of 20°C/min was used for the analysis. Assuming a first-order reaction mechanism (n = 1), the Coats–Redfern equation was linearized in the form:

$$\ln\left(\frac{-\ln(1-\alpha)}{T^2}\right) = \ln\left(\frac{AR}{\beta E\alpha}\right) - \frac{E_a}{RT} \quad (3.4)$$

$$\alpha = \frac{n}{m-n} \quad (3.5)$$

m0-mf

A linear plot of $\ln[-\ln(1-\alpha)/T^2]$ versus $1/T$ yielded a straight line with a correlation coefficient of $R^2 = 0.94$, indicating good model fitting (Figure 8). From the slope of the line, the calculated activation energy was 38.63 kJ/mol, suggesting that the thermal decomposition proceeds via a relatively low-energy pathway. This moderate activation energy implies that the decomposition and crystallization processes in the CuO–ZnO system are energy-efficient, which is advantageous for green synthesis and photocatalytic applications.

3.3.2 Results of Vibrational Energy Analysis of Chemical Bonds Using FTIR

The FTIR spectral analysis results of the synthesized composite are shown in Figure 9 and Table 3. For the sample dried at 120°C, the FTIR spectrum revealed the presence of the following functional group peaks: O–H stretching vibrations of the carboxyl group at 3454 cm^{-1} and 3832 cm^{-1} ; C–H bending vibration at 2315 cm^{-1} ; and carboxyl-related C–O stretching vibrations at 1416 cm^{-1} and 1575 cm^{-1} . These functional groups likely originate from the decomposition of the $-\text{CH}_3\text{COO}^-$ group in $\text{Cu}(\text{CH}_3\text{COO})_2 \cdot \text{H}_2\text{O}$ [34]. The Cu–O stretching vibration is observed at 636 cm^{-1} , while Zn–O bonds appear at 468 cm^{-1} and 574 cm^{-1} . For the sample dried at 500°C, the FTIR spectrum shows O–H stretching of the carboxyl group at 3435 cm^{-1} , C–H bending vibration at 2806 cm^{-1} , and stretching vibrations of the C–O and C=O bonds at 1625 cm^{-1} and 1115 cm^{-1} , respectively. The decomposition of zinc acetate used in the synthesis results in the formation of C=O and C–H bonds. The Cu–O stretching vibration is observed at 876 cm^{-1} , while the Zn–O bond is found at 445 cm^{-1} . The CuO–ZnO composite exhibits stretching vibrations in the 700–1100 cm^{-1} range, where metal oxides typically show strong absorption in the fingerprint region [29]. From these results, it can be concluded that citric acid forms coordination bonds with metal ions through its carboxyl groups. Additionally, at 120°C, the decomposition of copper sulfate has initiated, while further heating to 500°C leads to the decomposition of zinc acetate, the precursor of ZnO.

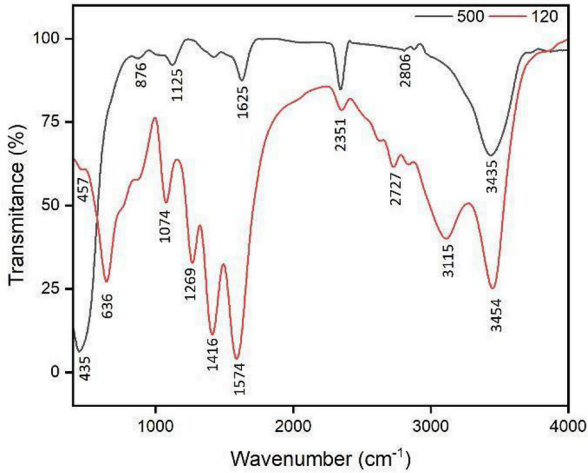


Fig. 9. FTIR analysis results of samples dried at 120°C and 500°C, respectively.

This is evidenced by the formation of Zn–O bonds and the appearance of C–O and C=O bonds resulting from the breakdown of the CH_3COO^- group.

Table 3. Interpretation of wavenumber assignments in FTIR analysis.

Bonds	Reference	Experiment results		Mode of vibration
		120°C	500°C	
-O-H	3200-3500 [28]	3454, 3832	3435	stretching vibration
C-H	2320 [35]	2351	2806	bending vibration
C-O	1600-1640 [36]	1416, 1574	1625	stretching vibration
C=O	1100-1500 [30]	1074, 1269	1125	
Cu-O	624 [31]	636	876	stretching vibration
Zn-O	400-590 [35]	468, 574	445	

3.3.3. Results of Crystalline Structure Determination Using XRD

Analysis The XRD analysis results of the CuO–ZnO composite are presented in Figure 10. X-ray diffraction (XRD) patterns were recorded using a [Shimadzu Maxima 7000] with Cu $K\alpha$ radiation ($\lambda = 1.5406 \text{ \AA}$), operating at [40 kV, 30 mA] over a 2θ range of [20– 80°] with a step size of [0.02°]. The raw diffraction data were processed using OriginPro 2024 software with baseline correction, $K\alpha_2$ stripping, and pseudo-Voigt peak fitting. Peak positions were identified by comparison with reference data from the ICDD PDF-4+ database (ZnO: #36-1451, CuO: #45-0937). Phase identification was carried out by matching the observed diffraction peaks to the

characteristic (hkl) reflections of each phase. For the sample dried at 120°C, the diffraction pattern showed weak peaks corresponding to CuO (110) at 32.2° and ZnO (002, 102) at 35.9° and 47.4°, which indicated an amorphous structure with emerging crystalline phases. Compared to standard reference values, these peaks indicate an amorphous structure, as a well-defined crystalline structure is not observed at this stage. However, the sample dried at 500°C exhibits a more developed crystalline structure. According to the JCPDS card No. 36-1451, the sample exhibits three primary peaks corresponding to the (100), (002), and (101) planes at 2 θ angles of 31.8°, 34.4°, and 36.3°, respectively. These peaks confirm the presence of a hexagonal wurtzite structure. The ZnO phase is characterized by diffraction peaks at 2 θ values of

31.8°, 34.5°, 36.4°, 47.6°, 62.9°, and 69.2°, corresponding to the (100), (002), (101), (102), (103), and (201) planes.

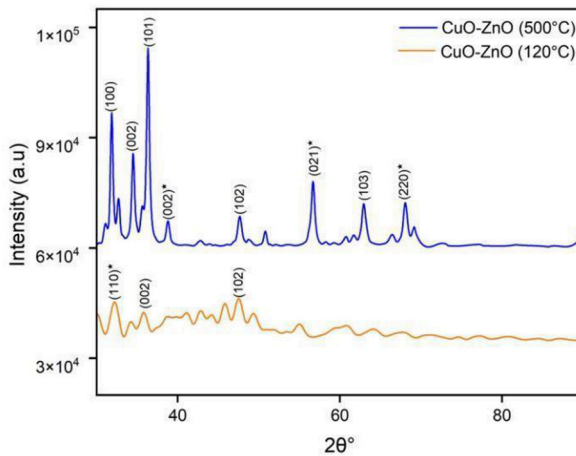


Fig. 10. XRD analysis result.

For the CuO phase, diffraction peaks are observed at 2 θ values of 32.7°, 38.9°, 56.7°, and 68.1°, corresponding to the (110), (002), (021), and (220) planes, respectively. Compared to standard reference values, copper oxide is confirmed to have a monoclinic crystal structure. In the XRD pattern, the CuO peaks are marked with an asterisk. No significant peak shifts were observed in the lattice planes compared to standard values, suggesting that the particles are likely spherical in shape. Relative quantification was done using intensity ratios of the strongest peaks. Additional support for phase assignment was provided by FTIR (Zn–O and Cu–O bond vibrations) and Raman spectroscopy, which confirmed the coexistence of both phases. Together, these complementary techniques validate the successful formation of CuO–ZnO composites.

The composition of metal oxide materials is generally proportional to the highest intensity peak in the diffraction pattern. The intensity ratio of CuO (I_{CuO}) and

ZnO (I_{ZnO}) can be used to estimate the relative concentrations of CuO (R_{CuO}) and ZnO (R_{ZnO}) in the composite using the following expressions:

$$R = \frac{I_{CuO}}{I_{CuO} + I_{ZnO}} \times 100\%$$

$$R = \frac{I_{ZnO}}{I_{CuO} + I_{ZnO}} \times 100\%$$

The highest intensity peaks for I_{CuO} and I_{ZnO} correspond to the (021) and (101) planes, respectively. The relative concentrations of CuO and ZnO in the composite were calculated to be 40.33% and 59.67%, respectively. The XRD-derived ratio (~40/60) is discussed alongside the feed-based theoretical composition (~17/83 wt%). which can be explained by the preferred orientation of ZnO crystallites, differences in crystallite size/strain, and microabsorption by CuO. We therefore report the XRD-derived values as approximate estimates and discuss them alongside the theoretical precursor-based composition.

Based on the analytical results, crystallinity increased significantly when the temperature was raised from 120°C to 500°C. Amorphous structures can undergo crystallization under thermal treatment [36]. A sharp exothermic peak observed in the DTA curve indicates the transition from amorphous to crystalline phase [37]. Comparison of morphological and XRD results indicates that particle aggregation led to the formation of a hexagonal structure. This approach assumes negligible preferred orientation and similar crystallite sizes for both phases, and therefore provides only an approximate estimation of phase composition.

4 Conclusions

In this study, a CuO–ZnO composite powder was synthesized using the sol-gel method. According to the UV-Visible spectrometry results, the composite exhibited an absorption peak at 373 nm. Raman spectroscopy analysis showed peaks at 278 cm^{-1} , 416 cm^{-1} , 564 cm^{-1} , and 1096 cm^{-1} , indicating the formation of the CuO–ZnO composite. Structural and morphological analysis revealed that the particles formed spherical-shaped composites with an average size of approximately 13.8 nm due to aggregation. Thermal analysis showed that moisture loss and the decomposition of organic substances occurred between 280°C and 400°C, and crystalline structures began to form at 500°C. FTIR analysis showed that as the temperature increased, bond stretching decreased, and CuO–ZnO bonding occurred through C–O and C=O bonds. XRD analysis revealed that the sample dried at 120°C had an amorphous structure, while increasing the heating temperature led to the formation of monoclinic CuO and hexagonal ZnO structures. The activation energy calculated by the Coats–Redfern method (38.63 kJ/mol) demonstrated moderate

thermal stability, supporting efficient photocatalytic phase development with minimal energy input. These characteristics position the CuO–ZnO composite as a promising material for green photocatalytic applications such as wastewater treatment and environmental decontamination. Future work will aim to enhance visiblelight absorption by incorporating Cu₂O phases or other dopants, optimizing the material for broader applications in sustainable environmental technologies.

Acknowledgments. This work has been done within the framework of the project (EUTOUG/20240103757) supported by the Erdenet Mining Corporation, the Erdenet Institute of Technology, and the National University of Mongolia. The valuable support of the project (J11B16) supported by the MJED is also highly appreciated.

5 References

- [1] M. Ismail et al., “Pollution, Toxicity and Carcinogenicity of Organic Dyes and their Catalytic Bio-Remediation,” *Curr Pharm Des*, vol. 25, no. 34, pp. 3645–3663, Nov. 2019, doi: 10.2174/1381612825666191021142026.
- [2] L. Persson et al., “Outside the Safe Operating Space of the Planetary Boundary for Novel Entities,” *Environ Sci Technol*, vol. 56, no. 3, pp. 1510–1521, Feb. 2022, doi: 10.1021/acs.est.1c04158.
- [3] E. ; S. N. , E. Pelizzetti, *Photocatalysis: Fundamentals and Applications*; Wiley, vol. Vol 52. New York, NY, USA, 1989.
- [4] A. Di Paola, L. Palmisano, and V. Augugliaro, “Photocatalytic behavior of mixed WO₃/WS₂ powders,” *Catal Today*, vol. 58, no. 2–3, pp. 141–149, May 2000, doi: 10.1016/S09205861(00)00249-2.
- [5] Q. Zhang et al., “CuO nanostructures: Synthesis, characterization, growth mechanisms, fundamental properties, and applications,” *Prog Mater Sci*, vol. 60, pp. 208–337, Mar. 2014, doi: 10.1016/j.pmatsci.2013.09.003.
- [6] Z. Haghparas, Z. Kordrostami, M. Sorouri, M. Rajabzadeh, and R. Khalifeh, “Highly sensitive non-enzymatic electrochemical glucose sensor based on dumbbell-shaped double-shelled hollow nanoporous CuO/ZnO microstructures,” *Sci Rep*, vol. 11, no. 1, p. 344, Jan. 2021, doi: 10.1038/s41598-020-79460-2.
- [7] O. Madelung, *Semiconductors: data handbook*, 3rd ed. 2004.
- [8] Z. Yang, J. Xu, W. Zhang, A. Liu, and S. Tang, “Controlled synthesis of CuO nanostructures by a simple solution route,” *J Solid State Chem*, vol. 180, no. 4, pp. 1390–1396, Apr. 2007, doi: 10.1016/j.jssc.2007.02.008.
- [9] Z. L. Wang, “Nanostructures of zinc oxide,” *Materials Today*, vol. 7, no. 6, pp. 26–33, Jun. 2004, doi: 10.1016/S1369-7021(04)00286-X.
- [10] E. Sonmez, S. Aydin, M. Yilmaz, M. T. Yurtcan, T. Karacali, and M. Ertugrul, “Study of Structural and Optical Properties of Zinc Oxide Rods Grown on Glasses by Chemical Spray Pyrolysis,” *J Nanomater*, vol. 2012, pp. 1–5, 2012, doi: 10.1155/2012/950793.
- [11] R. Saravanan, S. Karthikeyan, V. K. Gupta, G. Sekaran, V. Narayanan, and A. Stephen, “Enhanced photocatalytic activity of ZnO/CuO nanocomposite for the degradation of textile

- dye on visible light illumination,” *Materials Science and Engineering: C*, vol. 33, no. 1, pp. 91–98, Jan. 2013, doi: 10.1016/j.msec.2012.08.011.
- [12] B. Li and Y. Wang, “Facile synthesis and photocatalytic activity of ZnO–CuO nanocomposite,” *Superlattices Microstruct*, vol. 47, no. 5, pp. 615–623, May 2010, doi: 10.1016/j.spmi.2010.02.005.
- [13] Babak Sadeghi, *Synthesis and Application of Nanorods*. 2012.
- [14] G. Wisz, I. Virt, P. Sagan, P. Potera, and R. Yavorskyi, “Structural, Optical and Electrical Properties of Zinc Oxide Layers Produced by Pulsed Laser Deposition Method,” *Nanoscale Res Lett*, vol. 12, no. 1, p. 253, Dec. 2017, doi: 10.1186/s11671-017-2033-9.
- [15] S. J. P. C. Jagadish, “Zinc oxide bulk, thin films and nanostructures processing, properties and applications,” C. Jagadish, S.J. Pearton, 2006.
- [16] U. Ö. H. Morkoc, *Zinc Oxide: Fundamentals, Materials and Device Technology*. 2008.
- [17] R. Ciriminna, A. Fidalgo, V. Pandarus, F. Béland, L. M. Ilharco, and M. Pagliaro, “The Sol–Gel Route to Advanced Silica-Based Materials and Recent Applications,” *Chem Rev*, vol. 113, no. 8, pp. 6592–6620, Aug. 2013, doi: 10.1021/cr300399c.
- [18] D. R. Smith and M. Nordberg, “General Chemistry, Sampling, Analytical Methods, and Speciation*,” in *Handbook on the Toxicology of Metals*, Elsevier, 2015, pp. 15–44. doi: 10.1016/B9780-444-59453-2.00002-0.
- [19] H. Guo, M. Yin, N. Dong, M. Xu, L. Lou, and W. Zhang, “Effect of heat-treatment temperature on the luminescent properties of Lu₂O₃:Eu film prepared by Pechini sol–gel method,” *Appl Surf Sci*, vol. 243, no. 1–4, pp. 245–250, Apr. 2005, doi: 10.1016/j.apsusc.2004.09.069.
- [20] Q. Chen, Y. Wang, M. Zheng, H. Fang, and X. Meng, “Nanostructures confined self-assembled in biomimetic nanochannels for enhancing the sensitivity of biological molecules response,” *Journal of Materials Science: Materials in Electronics*, vol. 29, no. 23, pp. 19757–19767, Dec. 2018, doi: 10.1007/s10854-018-0101-2.
- [21] J. X. Wang et al., “Free-standing ZnO–CuO composite nanowire array films and their gas sensing properties,” *Nanotechnology*, vol. 22, no. 32, p. 325704, Aug. 2011, doi: 10.1088/09574484/22/32/325704.
- [22] M. Pandey et al., “Targeted and Enhanced Antimicrobial Inhibition of Mesoporous ZnO–Ag₂O/Ag, ZnO–CuO, and ZnO–SnO₂ Composite Nanoparticles,” *ACS Omega*, vol. 6, no. 47, pp. 31615–31631, Nov. 2021, doi: 10.1021/acsomega.1c04139.
- [23] K. G. Krishna, S. R. Parne, and P. Nagaraju, “An optical study of heterojunction n-ZnO/p-CuO nanosheets and detection of n-butanol vapour at room temperature,” *J Mater Sci*, vol. 58, no. 40, pp. 15660–15675, Oct. 2023, doi: 10.1007/s10853-023-08997-0.
- [24] J. Fang and Y. Xuan, “Investigation of optical absorption and photothermal conversion characteristics of binary CuO/ZnO nanofluids,” *RSC Adv*, vol. 7, no. 88, pp. 56023–56033, 2017, doi: 10.1039/C7RA12022B.
- [25] S. Ghorbani, R. Sh. Razavi, M. R. Loghman-Estarki, and A. Alhaji, “Development of MgO–Y₂O₃ Composite Nanopowder by Pechini Sol–Gel Method: Effect of Synthesis Parameters on Morphology, Particle Size, and Phase Distribution,” *J Clust Sci*, vol. 28, no. 3, pp. 1523–1539, May 2017, doi: 10.1007/s10876-017-1162-8.
- [26] M. M. Thackeray, M. F. Mansuetto, and J. B. Bates, “Structural stability of LiMn₂O₄ electrodes for lithium batteries,” *J Power Sources*, vol. 68, no. 1, pp. 153–158, Sep. 1997, doi:

- 10.1016/S0378-7753(96)02624-9.
- [27] A. Llusco, M. Grageda, and S. Ushak, “Kinetic and Thermodynamic Studies on Synthesis of Mg-Doped LiMn₂O₄ Nanoparticles,” *Nanomaterials*, vol. 10, no. 7, p. 1409, Jul. 2020, doi: 10.3390/nano10071409.
- [28] A. Atri, M. Echabaane, A. Bouzidi, I. Harabi, B. M. Soucase, and R. Ben Chaâbane, “Green synthesis of copper oxide nanoparticles using Ephedra Alata plant extract and a study of their antifungal, antibacterial activity and photocatalytic performance under sunlight,” *Heliyon*, vol. 9, no. 2, p. e13484, Feb. 2023, doi: 10.1016/j.heliyon.2023.e13484.
- [29] S. Faisal et al., “Green Synthesis of Zinc Oxide (ZnO) Nanoparticles Using Aqueous Fruit Extracts of *Myristica fragrans*: Their Characterizations and Biological and Environmental Applications,” *ACS Omega*, vol. 6, no. 14, pp. 9709–9722, Apr. 2021, doi: 10.1021/acsomega.1c00310.
- [30] D. Renuga, J. Jeyasundari, A. S. Shakthi Athithan, and Y. Brightson Arul Jacob, “Synthesis and characterization of copper oxide nanoparticles using *Brassica oleracea* var. *italic* extract for its antifungal application,” *Mater Res Express*, vol. 7, no. 4, p. 045007, Apr. 2020, doi: 10.1088/2053-1591/ab7b94.
- [31] Y. Hu and Y. Wang, “Cuprous oxide nanoparticles selectively induce apoptosis of tumor cells,” *Int J Nanomedicine*, p. 2641, May 2012, doi: 10.2147/IJN.S31133.
- [32] S. R. Naqvi et al., “Pyrolysis of high ash sewage sludge: Kinetics and thermodynamic analysis using Coats-Redfern method,” *Renew Energy*, vol. 131, pp. 854–860, Feb. 2019, doi: 10.1016/j.renene.2018.07.094.
- [33] M. Raza, B. Abu-Jdayil, A. H. Al-Marzouqi, and A. Inayat, “Kinetic and thermodynamic analyses of date palm surface fibers pyrolysis using Coats-Redfern method,” *Renew Energy*, vol. 183, pp. 67–77, Jan. 2022, doi: 10.1016/j.renene.2021.10.065.
- [34] D. Saravanakkumar et al., “Synthesis and characterization of ZnO–CuO nanocomposites powder by modified perfume spray pyrolysis method and its antimicrobial investigation,” *Journal of Semiconductors*, vol. 39, no. 3, p. 033001, Mar. 2018, doi: 10.1088/1674-4926/39/3/033001.
- [35] S. Faisal et al., “Green Synthesis of Zinc Oxide (ZnO) Nanoparticles Using Aqueous Fruit Extracts of *Myristica fragrans*: Their Characterizations and Biological and Environmental Applications,” *ACS Omega*, vol. 6, no. 14, pp. 9709–9722, Apr. 2021, doi: 10.1021/acsomega.1c00310.
- [36] A. E. E. and S. A. Miray Çelikkilek, “Crystallization Kinetics of Amorphous Materials ,” *InTech*, Apr. 2012.
- [37] J. Maletaskic et al., “Synthesis and characterization of monophase CaO-TiO₂-SiO₂ (sphene) based glass-ceramics,” *Science of Sintering*, vol. 52, no. 1, pp. 41–52, 2020, doi: 10.2298/SOS2001041M.
- [38] O. Monfort and Y. Wu, “Photocatalytic Processes for Environmental Applications,” *Processes*, vol. 9, no. 11, p. 2080, Nov. 2021, doi: 10.3390/pr9112080.
- [39] P. Wang, B. Huang, Y. Dai, and M.-H. Whangbo, “Plasmonic photocatalysts: harvesting visible light with noble metal nanoparticles,” *Physical Chemistry Chemical Physics*, vol. 14, no. 28, p. 9813, 2012, doi: 10.1039/c2cp40823f.

- [40] J. Lunee, N. Tserendulam, and E. Norov, “Synergistic antibacterial activity of ciprofloxacin-loaded silver and mesoporous silica core/shell nanoparticles,” *Mongolian Journal of Engineering and Applied Sciences*, vol. 7, no. 1, May 2025, doi: 10.22353/mjeas.v7i1.9635.

Open Access This chapter is licensed under the terms of the Creative Commons Attribution-NonCommercial 4.0 International License (<http://creativecommons.org/licenses/by-nc/4.0/>), which permits any noncommercial use, sharing, adaptation, distribution and reproduction in any medium or format, as long as you give appropriate credit to the original author(s) and the source, provide a link to the Creative Commons license and indicate if changes were made.

The images or other third party material in this chapter are included in the chapter's Creative Commons license, unless indicated otherwise in a credit line to the material. If material is not included in the chapter's Creative Commons license and your intended use is not permitted by statutory regulation or exceeds the permitted use, you will need to obtain permission directly from the copyright holder.

